Continental Shelf Research 167 (2018) 46–54

Contents lists available at ScienceDirect

Continental Shelf Research

journal homepage: www.elsevier.com/locate/csr

Observations of semidiurnal internal tides on the Patagonian Shelf

Tianyi Zhang[a,*], Alexander E. Yankovsky[a], Alberto R. Piola[b], Daniel Valla[b]

[a] School of the Earth, Ocean and Environment, University of South Carolina, Columbia, SC 29208, USA
[b] Departamento Oceanografía, Servicio de Hidrografía Naval and Departamento de Ciencias de la Atmosfera y los Océanos, Universidad de Buenos Aires, and UMI/IFAECI, CONICET, Av. Montes de Oca 2124, 1271 Ciudad de Buenos Aires, Argentina

ARTICLE INFO

Keywords:
Internal waves
Tides
Refraction
Mean current
Patagonian Shelf
The Malvinas Current

ABSTRACT

The Patagonian Shelf in the western South Atlantic is known for strong semidiurnal tides and intense seasonal stratification. Both observations and models reveal substantial cross-isobath tidal energy fluxes at the shelf break between 44 and 41°S. These conditions are potentially favorable for internal wave generation, but global tidal models do not show significant baroclinic energy radiation from this region. A possible explanation for the lack of offshore radiation is explored through analyzing the data from two moorings deployed along the Patagonian shelf break. At both mooring sites, the velocity spectra reveal strong baroclinic oscillations at the semidiurnal frequency with a vertical structure resembling the first mode. Unlike barotropic tides with strong cross-isobath polarization, the baroclinic tidal ellipses are less polarized. Internal tide propagation is delineated by estimating a proxy for the baroclinic energy flux, which is the product of band-passed baroclinic velocity near the bottom and temperature at mid-depth. The proxy vectors show that internal tide propagation is highly sensitive to the strength of the Malvinas Current propagating northward over the continental slope. When the mean current becomes stronger, the proxy vectors turn southward, pointing upstream of the Malvinas Current direction. It is concluded that the presence of an energetic western boundary current reduces the offshore radiation of internal tides, likely due to the wave refraction on the mean current.

1. Introduction

Semidiurnal tidal waves propagating along continental margins are strongly affected by wide continental shelves (e.g., Ke and Yankovsky, 2010; Zhang and Yankovsky, 2016): the across-shelf wave structure no longer resembles an analytical Kelvin wave solution and concentrates over the variable topography, while both the phase speed and group velocity are substantially reduced compared to long gravity waves in the open ocean. Furthermore, these modified Kelvin waves are very sensitive to alongshore changes of continental shelf topography. When shelf width changes in the alongshore direction, the alongshore energy flux on the shelf becomes divergent and results in compensating cross-isobath energy flux farther offshore, over the continental slope. The combination of cross-isobath barotropic velocities at the shelf break and a stratified water column results in the radiation of internal waves (IWs). Under favorable conditions, 15% or more of the incident barotropic tidal energy flux can radiate as IWs (Yankovsky and Zhang, 2017).

One of the regions in the World Ocean which fits this scenario is the Patagonian Shelf (PS) in the southwestern Atlantic Ocean. The Patagonian continental shelf extends from the southeastern tip of South America (55°S) to ~ 40°S. North of the Malvinas Islands, the shelf width of the PS is more than 500 km, and gradually narrows in the downstream direction to less than 200 km at 38°S. Water depth increases to over 4 km in the open ocean across the 200 km wide continental slope. The Patagonian Shelf is known for energetic semidiurnal tides propagating along the shelf (e.g., Webb, 1973; Kantha et al., 1995; Glorioso and Flather, 1997). Palma's et al. (2004) numerical study found strong M_2 tidal energy flux along and across the northern part of the PS where the shelf narrows, with associated tidal dissipation concentrated in the region. Water stratification in the PS area is characterized by a seasonal thermocline on the mid- and outer shelf (typical bottom depths of 100–200 m), which is significantly weaker during the austral winter (e.g., Martos and Piccolo, 1988; Rivas and Piola, 2002; Bianchi et al., 2009). The shelf is bounded offshore by the Malvinas Current (MC), a western boundary current carrying relatively cold sub-Antarctic water along the western margin of the Argentine Basin (e.g., Piola and Gordon, 1989). The transition between the shelf and the MC water is characterized by moderate cross-shore temperature and salinity gradients (e.g., Saraceno et al., 2004; Romero et al., 2006; Franco et al., 2008). At the shelf break (typical bottom depth of ~200 m) the stratification is somewhat weaker than observed farther onshore (Romero

* Corresponding author.
E-mail address: tzhang@geol.sc.edu (T. Zhang).

https://doi.org/10.1016/j.csr.2018.08.004
Received 21 December 2017; Received in revised form 23 May 2018; Accepted 9 August 2018
Available online 13 August 2018
0278-4343/

et al., 2006). Nonetheless, temperature and salinity records show the onset of a well-defined pycnocline in early November (Valla and Piola, 2015).

Strong stratification in the warm season and cross-isobath barotropic energy fluxes on the PS provide favorable conditions for internal tide generation. Early theoretical studies of internal tides (e.g., Baines, 1982) considered this region as one of the substantial contributors to global internal tidal energy production. However, due to the lack of observations of internal tides in the region, the barotropic to baroclinic energy conversion was not considered as a major source of barotropic dissipation on the PS. Later studies (e.g. Kantha et al., 1995; Glorioso and Flather, 1997) concluded that most of the tidal energy dissipates through bottom friction. Global internal tide model simulations (e.g. Simmons et al., 2004) found that primary regions of M_2 conversion into baroclinic modes in the South Atlantic Ocean are the Drake Passage and the Scotia Sea, south of the PS, whereas little conversion occurred at the Patagonian Shelf break.

IWs observed by satellite imaging (Jackson, 2007) and global altimetry data (Zhao et al., 2016) suggest that there is baroclinic energy radiation over the Patagonian continental slope. A comparison between observational and model data (Buijsman et al., 2015) shows that the global internal tide model predicts lower tidal dissipation on the PS than the dissipation inferred from the TPXO8-atlas model. A parameterized conversion (Buijsman et al., 2016) can significantly improve the contribution of internal tides to tidal dissipation off the continental slope, but the baroclinic wave drag is not applied on continental shelves due to the shallow water depth; thus the barotropic to baroclinic conversion on the PS remains unresolved.

It is possible that global internal tide models do not resolve the generation of internal tides at the PS due to insufficient spatial resolution. Palma et al. (2008) used a baroclinic model with a horizontal resolution of 5 km and 25 levels in the vertical to simulate the circulation responses to tides, shelf break fronts, and wind forcing, but the associated IW dynamics response was not reported. A recent study (Magalhães and da Silva, 2017) addresses IWs in the region, but of non-tidal origin. In their study, IWs are identified in high-resolution satellite images, and are suggested to be due to the resonant generation by the MC encountering topographic irregularities over a continental slope. The northward propagating MC has a strong flow of 0.4–0.7 m/s between 50°S to 43.5°S (Piola et al., 2013; Artana et al., 2016) and is therefore likely to influence the generation of IWs.

This study focuses on the semidiurnal internal tides in the PS region inferred from mooring data collected at the shelf break. The rest of the paper is organized as follows: Section 2 describes the collection and analysis of the data; Section 3 presents the results of data analysis; discussion of the possible influence of the MC on internal tides in the study area along with conclusions are presented in Section 4.

2. Data collection and analysis

Velocity and temperature time series were obtained from two mooring deployments (Valla and Piola, 2015) along the 200-m isobath at the shelf break (Fig. 1). Mooring data were collected from October 16 through December 5, 2005 at site A (43.820°S, 59.673°W), and from September 25, 2006 through March 8, 2007 at site B (40.987°S, 57.003°W). Both moorings measured the current velocity at hourly intervals with acoustic Doppler current profilers (ADCP). The current velocities were estimated from 10 m bins and recorded at 7 depth levels (10, 30, 50, 70, 100, 130, and 160 m), spanning nearly the entire water column. Temperature was recorded at 6 depth levels (1, 10, 30, 50, 75, and 100 m) at site A, whereas only near-surface (1 m) temperature was recorded at site B.

Historical CTD data were used to investigate the vertical density structure in the vicinity of the shelf break near the mooring sites. The data are available at the US NODC World Ocean Database 2013 http://www.nodc.noaa.gov/OC5/WOD/pr_wod.html (Boyer et al., 2013).

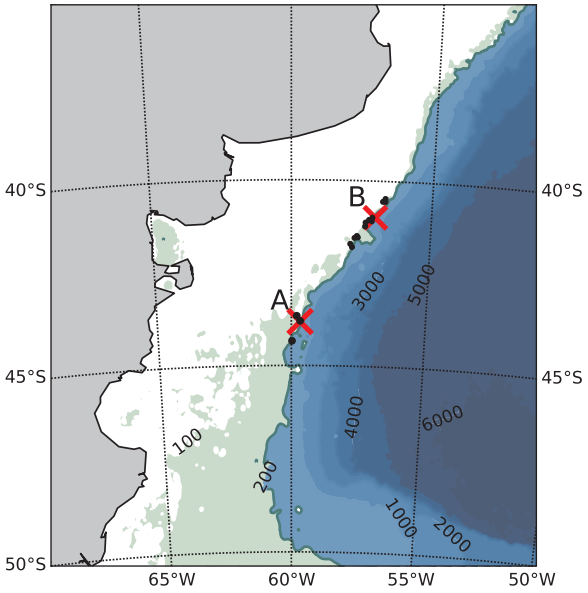

Fig. 1. Map of the study area showing bathymetry (in meters), locations of mooring sites (red crosses), and hydrographic stations (dots). (For interpretation of the references to colour in this figure legend, the reader is referred to the web version of this article.)

Hydrographic stations were selected within 100 km from each mooring site and within 11 km inshore from the 200-m isobath (Fig. 1). No data were selected at locations over the continental slope due to strong temperature and salinity gradients associated with the Malvinas Current (e. g., Romero et al., 2006; Piola et al., 2010). Furthermore, CTD profiles were selected for the seasons representing mooring deployments: the austral spring for site A and the austral spring-summer for site B. The selected hydrographic stations are summarized in Table 1 and all density profiles are shown in Fig. 2.

For site A, one of the three available stations was occupied during the actual mooring deployment as a part of the Global Environment Facility (GEF) Patagonia Project (Charo and Piola, 2014). At site B, available stations cluster in two groups, representing early austral spring (September–October) and late summer (February-March) (Fig. 2). Stations from late austral summer are characterized by a seasonal pycnocline within the uppermost 40 m. Profiles of buoyancy frequency N defined as $N^2 = -\frac{g}{\rho_0}\frac{d\rho_0}{dz}$ were estimated for all density profiles. Here, $\rho_0(z)$ is the density, z is the vertical coordinate (positive

Table 1
A summary of the locations and dates of hydrographic stations.

	Latitude	Longitude	Date
Site A			
1	− 43.6638	− 59.7982	9/9/2006
2	− 43.7983	− 59.6722	10/15/2005
3	− 44.338	− 59.974	11/5/1993
Site B			
1	− 41.0833	− 57.1257	2/8/1990
2	− 41.1233	− 57.345	3/23/1989
3	− 40.47	− 56.665	3/9/1994
4	− 41.544	− 57.725	3/10/1994
5	− 40.55	− 56.6667	3/22/1989
6	− 41.7083	− 57.875	3/23/1989
7	− 41.4917	− 57.645	9/5/1989
8	− 41.7932	− 57.8097	9/4/1997
9	− 41.5292	− 57.6095	9/5/1997
10	− 41.2292	− 57.3588	9/5/1997
11	− 41.049	− 57.225	10/10/2005
12	− 40.9883	− 57.1083	10/21/1997
13	− 40.55	− 56.7517	10/21/1997

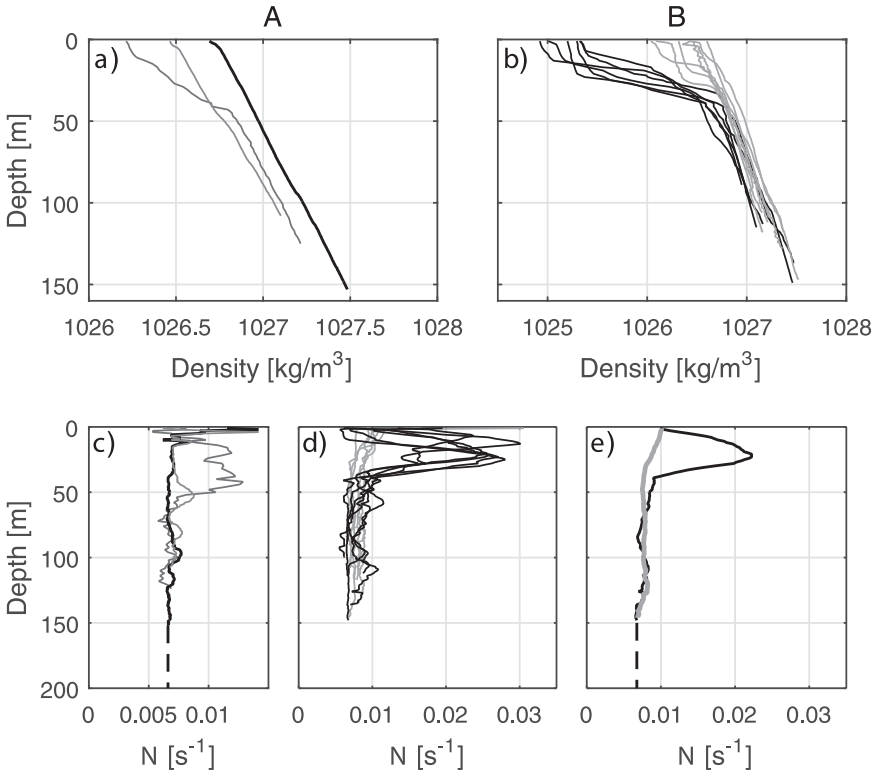

Fig. 2. Vertical profiles of density (top) and N (bottom) at sites A (*a* and *c*) and B (*b* and *d*). At site B, the grey and black lines represent austral early spring and late summer, respectively. Also shown are the averaged spring and late summer profiles of N at site B (*e*). The extrapolated constant values of N are shown as dashed lines.

upward), and g is the acceleration due to gravity. Both ρ_0 and N profiles were gridded in 1 m vertical bins, and N profiles were further smoothed by applying 10-m running average.

The observed N profiles were used to assess the IW properties. The IW dispersion characteristics and the normal mode vertical profiles were estimated by solving numerically the following boundary value problem (Pedlosky, 2003):

$$\frac{d^2w(z)}{dz^2} + K_H{}^2\frac{(N(z)^2-\omega^2)}{(\omega^2-f^2)}w(z) = 0 \tag{1}$$

$$w = 0, z = 0, -h, \tag{2}$$

where ω is the wave frequency, K_H is the horizontal wave number, h is the water depth, f is the inertial frequency, and w is the vertical velocity component. The eigenvalue K_{Hn} and the corresponding eigenvector $w_n(z)$ for the n^{th} normal mode were found for specified ω (representing the semidiurnal frequency) and $N(z)$. The derivatives in (1) were approximated with finite differences. The water depth was set at 200 m and the water column was discretized with 199 internal grid points.

Since eigenvectors of IW normal modes are expressed in terms of $w(z)$, they are converted into corresponding eigenvectors of the horizontal velocity component u (so that the comparison with mooring data can be made) through the continuity equation:

$$\nabla \bullet \vec{u} = 0, \tag{3}$$

where $\vec{u}$ is the velocity vector $\vec{u} = \vec{i}\,u + \vec{j}\,v + \vec{k}\,w$. Assuming for simplicity that the wave vector $\vec{K_H}$ is aligned with the x-axis, the nth mode eigenvector of the horizontal velocity component u is:

$$u_n(z) = \frac{1}{K_H}\frac{dw_n(z)}{dz} \tag{4}$$

With this orientation of the wave vector, $u_n(z)$ and $v_n(z)$ have the same vertical profiles, but the ratio of their amplitudes is ω/f. That is, the actual orientation of the horizontal wave vector is immaterial for the identification of IW modes in the observational data.

In the following analysis, we retain a standard decomposition of the horizontal velocity vector into its eastward u and northward v components, and do not refer to frequently used alongshelf and across-shelf components (as was done for instance by Valla and Piola, 2015). The main reason for this is that the IW velocity vectors (a primary focus of our study) do not reveal strong polarization, as will be shown below. The barotropic velocity component was calculated as depth-averaged of all 7 water layers recorded, from 10 m to 160 m. The baroclinic velocity component in each water layer was calculated as a difference between the observed velocity and the depth-averaged velocity. Spectral energy and cross-spectral coherence of the velocity components were calculated to analyze the signal strength at the semidiurnal frequency. The spectral analysis was performed by applying Fast Fourier Transform. Time series were subdivided into 512 h-long segments overlapping by 50%. Along with velocity components, temperature records at site A were also analyzed by means of the spectral analysis.

The semidiurnal tidal species in the time series were singled out by applying a band-pass Lanczos-cosine filter (Duchon, 1979) with frequency bands of $\Delta f = [f_{c1} = 1.3, f_{c2} = 3.3]$ cycles per day, where f_{c1} and f_{c2} are the high-pass and low-pass cut-off frequencies respectively. The Lanczos-cosine filter is defined by

$$\omega_k = \left(\frac{\sin(2\pi k f_{c2})}{k\pi} - \frac{\sin(2\pi k f_{c1})}{k\pi}\right)\frac{\sin\left(\frac{k\pi}{M}\right)}{k\pi/M}, \tag{5}$$

where $k = 1, 2, \ldots, M$. We used $M = 20$ as the total sum of weights. For chosen parameters, the filter efficiently eliminates the near inertial, as well as high frequency ($\omega > 3.5 \times 10^{-5}$ Hz) variability.

For band-passed velocity components, principal axis analysis (Freeland et al., 1975) was performed and revealed the tidal ellipses of barotropic and baroclinic velocity components.

The IW propagation can be characterized by the baroclinic energy flux, which is defined as

$$\overrightarrow{F}(z) = \overrightarrow{u}'_H(z)p'(z) \tag{6}$$

$$p'(z) = \int_z^{\eta} g[\rho(z) - \rho_0(z-\eta)]dz, \tag{7}$$

where $\overrightarrow{u}'_H(z)$ is the horizontal baroclinic velocity component, $p'(z)$ is the pressure perturbation, ρ is the instantaneous density, and η is the free surface perturbation. Since the vertical resolution in mooring data was too coarse for an accurate integration of (7), especially in the lower part of the water column, we constructed a proxy for the energy flux as follows. As the water column was primarily thermally stratified at site A (e.g., Bianchi et al., 2005), we used a band-passed temperature record in the middle of the water column at depth z_1 (taken with a minus sign) as a proxy for the density perturbation. Specifically, we selected z_1 corresponding approximately to the maximum of w_n (or, equivalently, the nodal point of u_n) in the first IW mode which, as will be shown below, dominated the IW response at the shelf break. For the horizontal velocity, we selected the depth z_2 below z_1 where the baroclinic velocity signal was strongest (near the bottom as will be subsequently shown). The energy flux proxy is thus defined as

$$\overrightarrow{F}' = -\hat{u}_H(z_2)\hat{T}(z_1), \tag{8}$$

where T is the temperature and the hat symbol refers to the band-passed time series.

3. Results

At site A, all density profiles reveal a near-constant buoyancy frequency ($N \sim 0.007\ s^{-1}$) below 70 m depth. Early in the spring season, N remains nearly constant throughout the water column, while later in the spring (November) N increases in the upper 50 m reaching 0.012–0.013 s^{-1} (Fig. 2c). Similarly, at site B, all profiles have a near-constant N below 50 m (~0.007–0.008 s^{-1}) regardless of the season, and a well-pronounced near surface maximum (~0.02–0.03 s^{-1}) for the late austral summer (Fig. 2d).

For calculating the IW properties at site A, the N profile sampled during the mooring deployment (heavy line in Fig. 2c) was utilized. For site B, available N profiles were averaged in two groups, representing austral early spring and late summer (Fig. 2e). Since the nominal depth of both mooring buoys was 200 m, N profiles were extrapolated to 200 m depth at constant values shown as dashed lines in Fig. 2c and e.

Vertical profiles of horizontal velocity for the three lowest IW modes at semidiurnal frequency corresponding to the three N profiles (site A, site B early spring, and site B late summer) are shown in Fig. 3. For both N profiles corresponding to the austral spring (Fig. 3a and b), normal modes closely resemble analytical solutions based on the constant N (e.g., Pedlosky, 2003): nodes are uniformly spaced in the vertical, while vertical profiles resemble a cosine function with constant amplitude. For the surface-intensified stratification of the late summer (Fig. 3c), normal modes exhibit moderate near-surface intensification (especially well pronounced for the first mode), while nodes in the upper 100 m also slightly shift upward. The phase speed $C = \omega/K_H$ for the first (gravest) mode varies from 0.45 m/s (site A) to 0.55 m/s (site B late summer).

The spectral analysis (Fig. 4) of the zonal and meridional velocity components shows a strong semidiurnal barotropic signal at both sites. The baroclinic signals at the semidiurnal frequency have mixed strengths. Near the bottom (160 m), the spectral energy of both u and v components at site A are of comparable intensity to the barotropic signal. In particular, the u component at A is weaker than the barotropic signal, whereas the v component is stronger, suggesting a possible change in the orientation of the tidal ellipse from barotropic to baroclinic modes. At site B, both u and v components are weaker than the barotropic signal; nonetheless, the spectral energy is still more than 10% of the barotropic signal.

At the near-surface level (10 m), the spectral energy of the baroclinic velocity exhibits very strong inertial signals, especially at site A, but somewhat weaker semidiurnal signals. Surface intensification of near-inertial oscillations suggests their wind-driven origin. All baroclinic semidiurnal signals at mid-depths are weaker than both surface and bottom signals and thus are not shown in Fig. 3. The relatively stronger velocity near the top and bottom of the water column at the semidiurnal frequency is in agreement with the theoretical structure of the first IW mode.

The spectral analysis reveals strong baroclinic components in velocity oscillations at diurnal, inertial and semidiurnal frequencies at both locations, likely associated with wave dynamics. While at diurnal and semidiurnal frequencies these oscillations are of tidal origin, the near inertial oscillations are wind-driven, their energy radiates downward

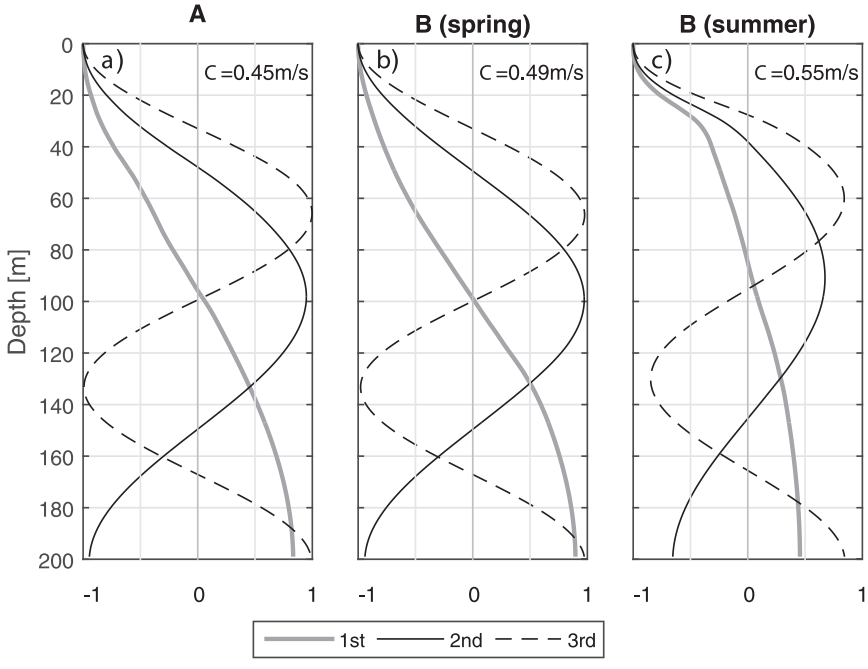

Fig. 3. Vertical profiles of horizontal velocity of the three lowest IW modes at mooring sites A (*a*) and B (*b*: spring and *c*: late summer).

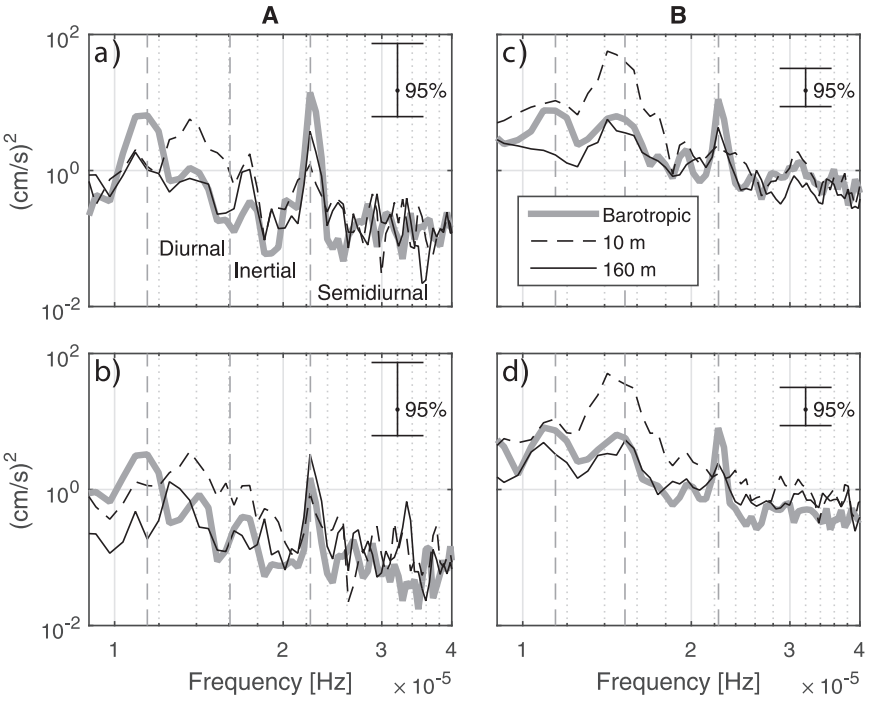

Fig. 4. Spectral energy of horizontal velocity components at mooring A (left column) and B (right column): *u*-component at A (*a*), *v*-component at A (*b*), *u*-component at B (*c*), and *v*-component at B (*d*).

and decays with depth (e.g., Rivas and Piola, 2011). At all three frequencies, the coherence (Fig. 5) between baroclinic velocities at 10 m and deeper layers is high, suggesting the presence of the lowest vertical modes. Among these three frequency bands, the semidiurnal oscillations have the highest coherence. At site A, the coherence is higher overall than at site B, but the structure is similar and hence is not shown.

Phase differences between the baroclinic velocity components at 10 m depth and deeper layers delineate the vertical structure of semidiurnal baroclinic oscillations (Fig. 6). At location A, the near-surface and near-bottom oscillations have approximately opposite phase (~ 180° phase difference), and the sign reversal occurs in the middle of the water column (Fig. 6a and b), where the phase difference exceeds 90°. This observed structure compares favorably with the first IW mode profile inferred from the CTD profiles (Fig. 3a). At site B, the *u* component resembles the structure in Fig. 6a, but the irregularity of phase difference (Fig. 6d) observed in the *v* component suggests that higher modes are present in the IW field. For both velocity components at site B, the phase reversal occurs at a shallower depth than at site A.

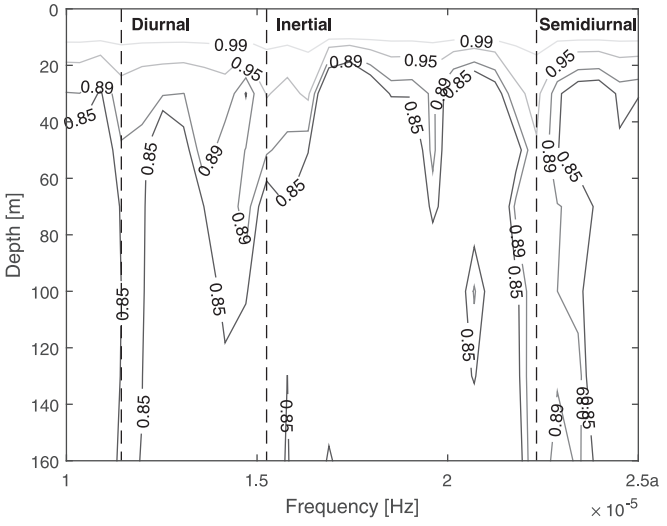

Fig. 5. Mooring B, coherence of baroclinic velocity component *u* between 10 m and 30, 50, 70, 100, 130 and 160 m bins. The 95% confidence interval of zero coherence is 0.28.

We further investigate the IW structure at sites A and B by estimating the spectral amplitudes of the baroclinic velocity components *u* and *v* at the semidiurnal frequency and normalizing them by the spectral amplitude of the barotropic velocity magnitude at the corresponding location (Fig. 7). The sign of the velocity components is determined from the phase difference shown in Fig. 6: the positive sign is assigned at the bottom and it is reversed to negative where the phase difference exceeds 90°. For comparison, we also plot the theoretical profile of the first IW mode at location A: at this site, the spectral amplitudes of the baroclinic velocities intensify in the upper and lower layers, and diminish at mid-depth. For site B, the velocity amplitudes do not show a clear decrease in the middle of the water column (especially for the *u*-component) indicating the presence of higher modes. The maximum baroclinic velocity components at both locations reach approximately 40–50% of the barotropic velocity magnitude at the semidiurnal frequency. A difference between the theoretical and observed distribution of velocity amplitude with depth is that the observed semidiurnal oscillations have a higher amplitude near the bottom, while for the predicted first mode the maximum velocity is at the surface. This discrepancy can be explained by the IW generation at the shelf break (near the bottom) and the contribution of higher modes. Overall, semidiurnal IWs at location B appear to have higher amplitude expressed as a fraction of the barotropic velocity amplitude compared to location A. This can be due to the different period of observations, which includes the summer season at site B.

Spectral analysis of temperature records at site A shows that semidiurnal oscillations are the most energetic in the superinertial frequency band indicating significant IW activity (Fig. 8). Overall, strong semidiurnal temperature signals are observed at mid-depth (50–100 m), consistent with the first mode structure. The maximum spectral energy is at 50 m and decreases at 100 m, which might be related to the development of a seasonal thermocline during the later stage of mooring

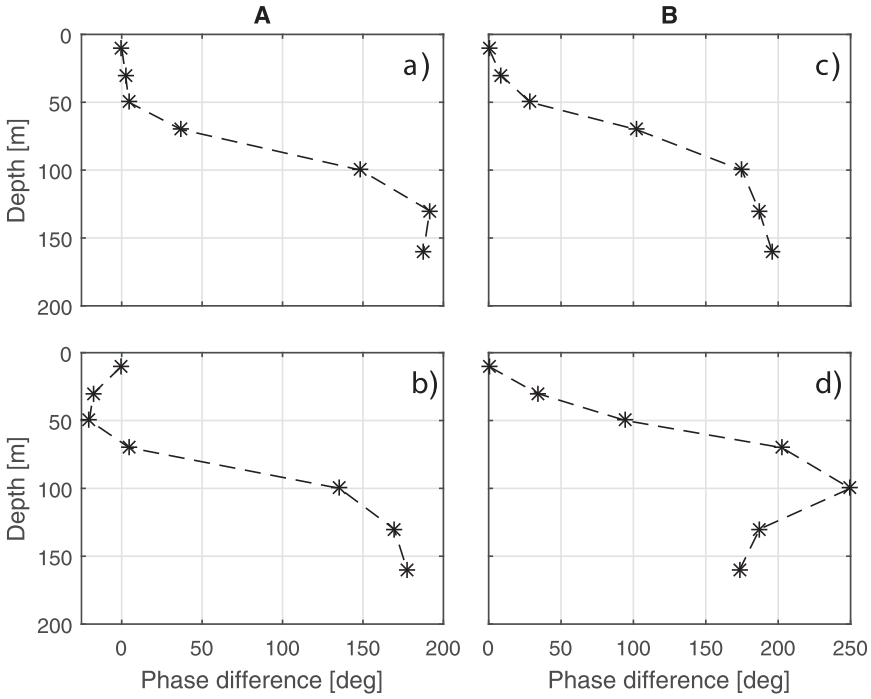

Fig. 6. Phase differences at the semidiurnal frequency between the near-surface and deeper bins for baroclinic velocity at mooring A (left column) and B (right column): *u*-component at A (*a*), *v*-component at A (*b*), *u*-component at B (*c*), and *v*-component at B (*d*).

deployment.

Further analysis is performed on band-passed time series of temperature, as well as barotropic and baroclinic velocity components, which retain only a semidiurnal frequency band (semidiurnal tidal species). The principal axis analysis of barotropic band-passed currents demonstrates that semidiurnal tidal ellipses are polarized in the cross-isobath direction (Fig. 9a and d). This result is consistent with regional numerical models of tidal dynamics (e.g., Glorioso and Flather, 1997). Baroclinic tidal currents are less polarized; near the surface (10 m depth), their principal axes are still oriented in a cross-isobath direction, but tidal ellipses are less elongated than in barotropic currents (Fig. 9b and e). The polarization of baroclinic tidal ellipses becomes even weaker in the near-bottom layer (Fig. 9c and f), and the principal axes are no longer oriented in the cross-isobath direction (especially at location B).

Lack of clear polarization of baroclinic tidal ellipses implies that there is no predominant direction for the internal tide propagation. We assess variations in the IW energy flux direction based on mooring records at location A (where the temperature data are available) by estimating the energy flux proxy (8). For z_1, we select 100 m depth (rather than 50 m) in order to minimize the influence of the atmospheric forcing on the temperature record. In addition, this depth corresponds to the maximum vertical velocity and isopycnal displacement in the first IW mode. For z_2, we select 160 m depth, where semidiurnal baroclinic currents are strongest. Proxy vectors are averaged over 12 h and sampled at a 1 h time interval; in addition, the original barotropic velocity (not band-passed) is averaged over the same 12 h intervals and is referred to as the mean current. The resulting mean current velocity magnitude values are binned in four equal groups separated by three quartiles. Proxy vectors in Fig. 10 are color-coded depending on the particular mean current group, which visualizes the mean current influence on the internal tide propagation. In addition, proxy vectors with x and y components both smaller than their corresponding standard deviations are discarded, which leaves only relatively strong signals depicted in Fig. 10.

Relatively few proxy vectors (and of a smaller magnitude) are oriented in the direction normal to local isobaths, pointing either inshore or offshore. This would be a preferential direction based on the theory of the IW generation by barotropic tides at the shelf break (e.g., Baines, 1982). A majority of proxy vectors have significant upstream (southward) component, against the MC direction. This tendency is especially obvious for proxy vectors with larger magnitudes (longer vectors in Fig. 10) and those corresponding to stronger mean current (magenta and red vectors). There are some proxy vectors pointing downstream

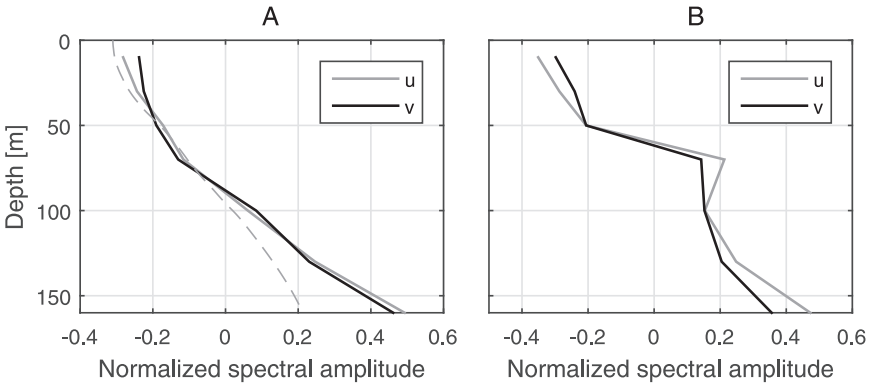

Fig. 7. Spectral amplitudes of *u* (grey) and *v* (black) baroclinic velocity components at the semidiurnal frequency, mooring A (left column) and B (right column). The amplitudes are normalized by the semidiurnal spectral amplitude of barotropic velocity magnitude from the corresponding mooring. The corresponding theoretical first mode profile for A is shown for comparison as a dashed line.

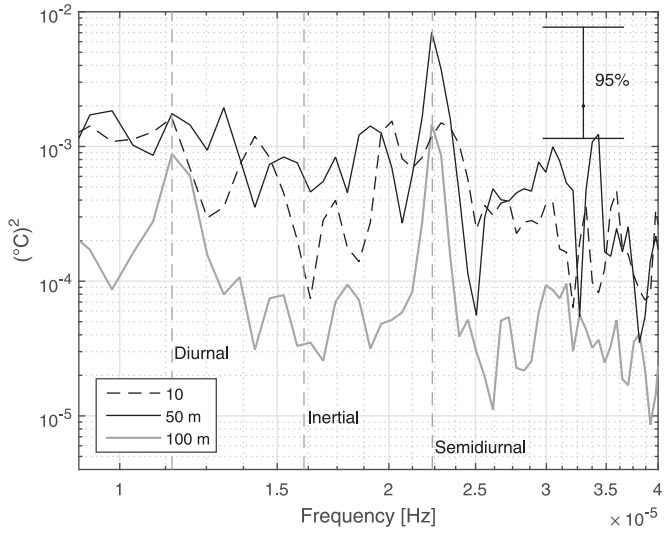

Fig. 8. Spectral energy of temperature at site A at 10, 50 and 100 m.

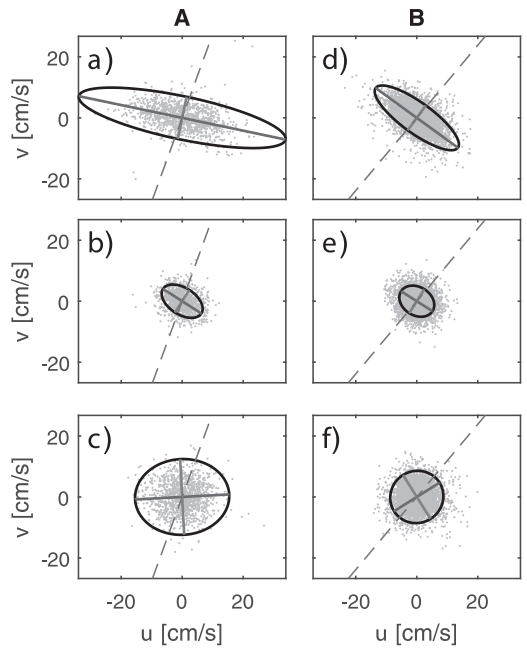

Fig. 9. Principal axis analysis of band-passed velocity records at mooring A (left column) and B (right column): barotropic velocity (*a*, *d*); baroclinic velocity at 10 m (*b*, *e*) and 160 m (*c*, *f*). Grey dots are velocity data; principal/minor axis is shown in black/grey. Dashed line indicates the shelf break orientation at the corresponding mooring site.

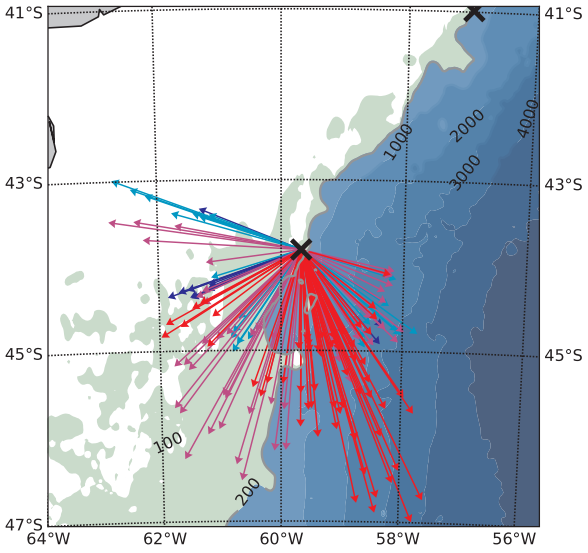

Fig. 10. Proxy vectors of the baroclinic energy fluxes at site A. Vector colors represent four groups of the mean current speed in the order of its increase: blue, cyan, magenta, and red.

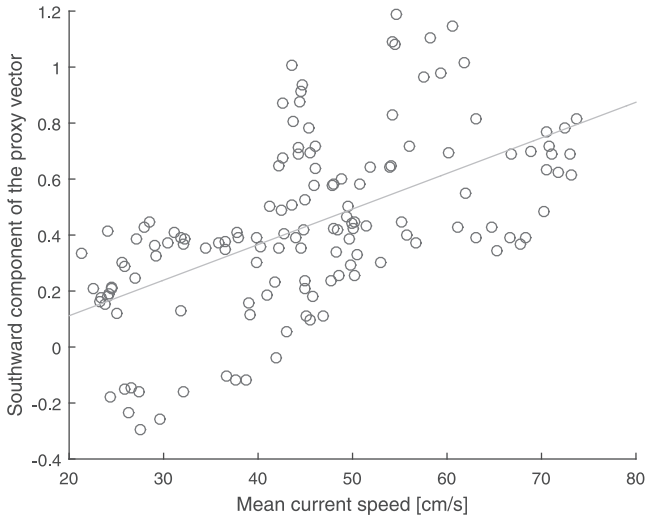

Fig. 11. Meridional component (positive southward) of the proxy vector versus the barotropic mean current speed. Linear regression is shown as a grey line.

(northeastward) but they are all of small magnitude falling below the screening threshold mentioned in the previous paragraph, and as such are not shown in Fig. 10. We conclude that the presence of the MC strongly affects the direction of the IW radiation from the Patagonian shelf break by deflecting IWs upstream relative to the MC direction.

We illustrate this conclusion by plotting the meridional component of proxy vectors against the mean current velocity magnitude (Fig. 11). The mean current velocity ranges from ~ 20 cm/s to over 70 cm/s so that during certain time intervals the mean current becomes supercritical relative to the IW phase speed. The proxy vector meridional component increases with the mean current speed, but the trend is not linear. The highest values of the southward proxy vector component correspond to the mean current speed ranging from 40 to 60 cm/s, when the mean current speed is comparable with the IW phase speed and the mean flow is in near-critical condition. Also, it should be noted that the proxy vector indicates the energy flux direction in the frame moving with the mean current. This implies that the actual direction of the IW propagation under supercritical conditions is to the north.

4. Discussion and conclusions

The Patagonian Shelf region is characterized by semidiurnal tides with both tidal amplitudes and dissipation rates being among the highest in the World Ocean, as shown by the satellite altimetry data analysis (e.g., Egbert and Ray, 2001). While barotropic semidiurnal tidal species in this region generally propagate northward, in the direction of Kelvin wave phase propagation, high resolution numerical models also reveal a strong onshore energy flux in the zonal band from 44°S to 41°S (e.g., Palma et al., 2004). Energetic cross-isobath tidal currents combined with a relatively strong seasonal stratification should lead to IW generation along the Patagonian shelf break (e.g., Baines, 1982), at least in its northern part, which is the study area for this paper. On the other hand, there is no evidence for internal tide radiation from this region into the open ocean in remotely-sensed data

(Zhao et al., 2016) and in numerical simulations (e.g., Simmons et al., 2004).

Our analysis of the current velocity and temperature time series from two moorings deployed along the 200-m isobath confirms the presence of strong semidiurnal internal tides. The spectral amplitude of the baroclinic velocity at the semidiurnal frequency near the bottom exceeds 40% of the corresponding barotropic velocity amplitude at both locations. The vertical profiles of the velocity spectra and phase difference suggest that internal tides at the shelf break are predominantly the first IW mode. However, unlike the theoretical first mode structure, the observed vertical structure of the baroclinic velocity at semidiurnal frequency is bottom-intensified, likely due to the contribution of higher modes.

The observed barotropic tidal currents are strongly polarized in the across-isobath direction. The baroclinic semidiurnal currents do not follow this pattern: the eccentricity of baroclinic tidal ellipses is smaller than in barotropic currents, especially near the bottom. Since the principal axis of baroclinic oscillations should be aligned with the horizontal wave vector when the wave frequency is higher than f (e.g., Pedlosky, 2003), the lack of polarization implies that there is no dominant direction for the semidiurnal IW radiation. By defining a proxy for the IW energy flux, we found that IW deflection from radiation across the isobaths is related to the mean current velocity magnitude: a stronger mean current causes IW energy to propagate southward, along the continental slope and upstream relative to the mean current direction. This pattern can result from the IW refraction on the mean current, when the wave vector turns in the direction of the minimal propagation speed, southward in our case.

Mean circulation in the study area is primarily associated with the Malvinas Current. Recent studies based on the analysis of shipboard surveys, satellite-tracked drifters, and remotely-sensed data (Piola et al., 2013), as well as on numerical modeling (e.g., Combes and Matano, 2014) revealed a rather complex structure of the MC, comprising multiple jets and hydrographic fronts (Franco et al., 2008). On average, two major jets can be identified; one is associated with the shelf break (~ 200 m isobath), and the other is at the continental slope plateau, where bottom slope has a local minimum (~ 1400-m isobath). Multiple jets tend to merge north of 45°S in averaged data with the MC core at the surface reaching 0.8–1 m/s between 1000- and 2000-m isobaths (Combes and Matano, 2014). However, instantaneous snapshots of the MC structure do show the presence of multiple jets and otherwise rich variability of the MC in our study area.

Barotropic tidally-averaged current speeds in the study area (site A) varied from ~0.2 to over 0.7 m/s, while the first IW mode phase speed ranged from ~0.45 m/s in the beginning of seasonal warming to ~0.55 m/s under the maximum seasonal stratification. Clearly, the mean current frequently reached a supercritical regime, exceeding the IW phase speed. As waves refract in the direction roughly parallel to the mean current, the existence of critical layers (where the mean current matches the IW phase speed) can in general inhibit IW propagation and lead to IW dissipation, turbulent mixing and homogenizing of the stratified water column (e.g., Baines, 1995). Even if IWs initially escape the deflecting effect of the mean current and radiate offshore when the mean current at the shelf break is weak, they are likely to refract and encounter a critical layer farther offshore, as they approach the maximum MC velocity. It also should be noted that the MC advects cold Antarctic water and thus the thermal stratification at its core is reduced (e.g., Piola et al., 2010), affecting the IW phase speed. We conclude that the overall impact of the MC on the internal tides generated at the shelf break in the study area is that their predominant propagation is in the along-shelf direction, which can lead to enhanced local dissipation.

The MC can directly generate IWs by interacting with along-shelf topographic irregularities, when the wavelength matches the length scale of the topographic feature. Such IWs were the subject of a recent study by Magalhães and da Silva (2017) and were evident in satellite images as trains of steep IWs propagating against the MC. Magalhães and da Silva (2017) argued that the observed waves were in a near-critical (transcritical in their terminology) regime. However, our analysis reveals that semidiurnal internal tides also propagate against the MC and their phase speed on many occasions nearly matches the mean current velocity. Hence, semidiurnal internal tides can also disintegrate into high-amplitude internal wave trains as they approach a near-critical regime and the two mechanisms for internal wave generation can be undistinguishable in the remotely sensed images reported by Magalhães and da Silva (2017). Unfortunately, in this study we could not analyze high frequency IWs and their possible link to the barotropic tidal forcing due to 1-h sampling interval of mooring records.

With a phase speed of ~0.5 m/s, semidiurnal IWs in the study area should have a wavelength of ~25 km. Their adequate resolution as they propagate along the shelf break will require a horizontal resolution of less than 5 km. Furthermore, the IW overturning and dissipation in the presence of a critical layer can be better represented in a non-hydrostatic model. It appears that global tidal models in their present configuration do not adequately resolve these dynamics. Nevertheless, these IWs can be important both in terms of barotropic tidal energy dissipation and turbulent mixing in the MC, as well as in other western boundary currents adjacent to broad continental shelves. Parameterization of these effects in numerical models merits future investigation.

Acknowledgements

This study was supported by the U.S. National Science Foundation through Grant OCE-1537449. The current meter observations were funded by Grant GEF-BIRF 28385-AR from the Global Environmental Facility. The authors are indebted to two anonymous reviewers for their insightful comments.

References

Artana, C., Ferrari, R., Koenig, Z., Saraceno, M., Piola, A.R., Provost, C., 2016. Malvinas Current variability from Argo floats and satellite altimetry. J. Geophys. Res. Oceans 121, 4854–4872. https://doi.org/10.1002/2016JC011889.

Baines, P.G., 1982. On internal tide generation models. Deep Sea Res. Part A Oceanogr. Res. Pap. 29, 307–338. https://doi.org/10.1016/0198-0149(82)90098-X.

Baines, P.G., 1995. Topographic Effects in Stratified Flows. Cambridge University Press, Cambridge, UK (482 pp).

Bianchi, A.A., Bianucci, L., Piola, A.R., Pino, D.R., Schloss, I., Poisson, A., Balestrini, C.F., 2005. Vertical stratification and air-sea CO_2 fluxes in the Patagonian shelf. J. Geophys. Res. 110, C07003. https://doi.org/10.1029/2004JC002488.

Bianchi, A.A., Pino, D.R., Perlender, H.G.I., Osiroff, A.P., Segura, V., Lutz, V., Clara, M.L., Balestrini, C.F., Piola, A.R., 2009. Annual balance and seasonal variability of sea-air CO_2 fluxes in the Patagonia Sea: their relationship with fronts and chlorophyll distribution. J. Geophys. Res. 114, C03018. https://doi.org/10.1029/2008JC004854.

Boyer, T.P., Antonov, J.I., Baranova, O.K., Coleman, C., Garcia, H.E., Grodsky, A., Johnson, D.R., Locarnini, R.A., Mishonov, A.V., O'Brien, T.D., Paver, C.R., Reagan, J. R., Seidov, D., Smolyar, I.V., Zweng, M.M., 2013. World Ocean Database 2013. (Report). NOAA Printing Office.

Buijsman, M.C., Ansong, J.K., Arbic, B.K., Richman, J.G., Shriver, J.F., Timko, P.G., Wallcraft, A.J., Whalen, C.B., Zhao, Z., 2016. Impact of Parameterized Internal Wave Drag on the Semidiurnal Energy Balance in a Global Ocean Circulation Model. J. Phys. Oceanogr. 46, 1399–1419. https://doi.org/10.1175/JPO-D-15-0074.1.

Buijsman, M.C., Arbic, B.K., Green, J.A.M., Helber, R.W., Richman, J.G., Shriver, J.F., Timko, P.G., Wallcraft, A., 2015. Optimizing internal wave drag in a forward barotropic model with semidiurnal tides. Ocean Model. 85, 42–55. https://doi.org/10.1016/j.ocemod.2014.11.003.

Charo, M., Piola, A.R., 2014. Hydrographic data from the GEF Patagonia cruises. Earth Syst. Sci. Data 6, 265.

Combes, V., Matano, R.P., 2014. A two-way nested simulation of the oceanic circulation in the Southwestern Atlantic. J. Geophys. Res. Oceans 119, 731–756. https://doi.org/10.1002/2013JC009498.

Duchon, C.E., 1979. Lanczos Filtering in One and Two Dimensions. J. Appl. Meteor. 1016–1022. https://doi.org/10.1175/1520-0450(1979)018<1016:LFIOAT>2.0.CO;2.

Egbert, G.D., Ray, R.D., 2001. Estimates of M2 tidal energy dissipation from TOPEX/Poseidon altimeter data. J. Geophys. Res. 106, 22475–22502. https://doi.org/10.1029/2000JC000699.

Franco, B.C., Piola, A.R., Rivas, A.L., Baldoni, A., Pisoni, J.P., 2008. Multiple thermal fronts near the Patagonian shelf break. Geophys. Res. Lett. 35, L02607. https://doi.org/10.1029/2007GL032066.

Freeland, H., Rhines, P., Rossby, T., 1975. Statistical observations of trajectories of

neutrally buoyant floats in North-Atlantic. J. Mar. Res. 33, 383–404.
Glorioso, P.D., Flather, R.A., 1997. The Patagonian Shelf tides. Progress. Oceanogr. Tidal Sci. Honour David E. Cartwright 40, 263–283. https://doi.org/10.1016/S0079-6611(98)00004-4.
Jackson, C., 2007. Internal wave detection using the Moderate Resolution Imaging Spectroradiometer (MODIS). J. Geophys. Res. 112, C11012. https://doi.org/10.1029/2007JC004220.
Kantha, L.H., Tierney, C., Lopez, J.W., Desai, S.D., Parke, M.E., Drexler, L., 1995. Barotropic tides in the global oceans from a nonlinear tidal model assimilating altimetric tides: 2. Altimetric Geophys. Implic. J. Geophys. Res. 100, 25309–25317. https://doi.org/10.1029/95JC02577.
Ke, Z., Yankovsky, A.E., 2010. The Hybrid Kelvin–Edge wave and its role in tidal dynamics. J. Phys. Oceanogr. 40, 2757–2767. https://doi.org/10.1175/2010JPO4430.1.
Magalhães, J., da Silva, J., 2017. Internal waves Along the Malvinas current: evidence of transcritical generation in satellite imagery. Oceanography 30. https://doi.org/10.5670/oceanog.2017.319.
Martos, P., Piccolo, M.C., 1988. Hydrography of the Argentine continental shelf between 38° and 42°S. Cont. Shelf Res. 8, 1043–1056. https://doi.org/10.1016/0278-4343(88)90038-6.
Palma, E.D., Matano, R.P., Piola, A.R., 2008. A numerical study of the Southwestern Atlantic Shelf circulation: stratified ocean response to local and offshore forcing. J. Geophys. Res. 113, C11010. https://doi.org/10.1029/2007JC004720.
Palma, E.D., Matano, R.P., Piola, A.R., 2004. A numerical study of the Southwestern Atlantic Shelf circulation: barotropic response to tidal and wind forcing. J. Geophys. Res. 109, C08014. https://doi.org/10.1029/2004JC002315.
Pedlosky, J., 2003. Waves in the Ocean and Atmosphere: Introduction to WaveDynamics, 2003 edition. Springer, Berlin, New York.
Piola, A.R., Franco, B.C., Palma, E.D., Saraceno, M., 2013. Multiple jets in the Malvinas Current. J. Geophys. Res. Oceans 118, 2107–2117. https://doi.org/10.1002/jgrc.20170.
Piola, A.R., Gordon, A.L., 1989. Intermediate waters in the southwest South Atlantic. Deep Sea Res. Part A Oceanogr. Res. Pap. 36, 1–16. https://doi.org/10.1016/0198-0149(89)90015-0.
Piola, A.R., Martínez Avellaneda, N., Guerrero, R.A., Jardón, F.P., Palma, E.D., Romero, S.I., 2010. Malvinas-slope water intrusions on the northern Patagonia continental shelf. Ocean Sci. 6, 345–359. https://doi.org/10.5194/os-6-345-2010.
Rivas, A.L., Piola, A.R., 2011. Near inertial oscillations at the shelf off northern Patagonia. Atlântica, Rio GrandeISSN 0102-1656, Rio Grande, Brasil, vol. 27, pp. 75–86. ⟨https://doi.org/10.5088/atlântica.v27i2.2172⟩.
Rivas, A.L., Piola, A.R., 2002. Vertical stratification at the shelf off northern Patagonia. Cont. Shelf Res. 22, 1549–1558. https://doi.org/10.1016/S0278-4343(02)00011-0.
Romero, S.I., Piola, A.R., Charo, M., Garcia, C.A.E., 2006. Chlorophyll-a variability off Patagonia based on SeaWiFS data. J. Geophys. Res. 111, C05021. https://doi.org/10.1029/2005JC003244.
Saraceno, M., Provost, C., Piola, A.R., Bava, J., Gagliardini, A., 2004. Brazil Malvinas Frontal System as seen from 9 years of advanced very high resolution radiometer data. J. Geophys. Res. 109, C05027. https://doi.org/10.1029/2003JC002127.
Simmons, H.L., Hallberg, R.W., Arbic, B.K., 2004. Internal wave generation in a global baroclinic tide model. Deep Sea Res. Part II: Top. Stud. Oceanogr. Small mesoscale Process. Their Impact Large Scale 51, 3043–3068. https://doi.org/10.1016/j.dsr2.2004.09.015.
Valla, D., Piola, A.R., 2015. Evidence of upwelling events at the northern Patagonian shelf break. J. Geophys. Res. Oceans 120, 7635–7656. https://doi.org/10.1002/2015JC011002.
Webb, D.J., 1973. On the age of the semi-diurnal tide. Deep Sea Res. Oceanogr. Abstr. 20, 847–852. https://doi.org/10.1016/0011-7471(73)90006-5.
Yankovsky, A.E., Zhang, T., 2017. Scattering of a Semidiurnal Barotropic Kelvin wave into internal waves over wide continental shelves. J. Phys. Oceanogr. 47, 2545–2562. https://doi.org/10.1175/JPO-D-16-0284.1.
Zhang, T., Yankovsky, A.E., 2016. On the nature of cross-isobath energy fluxes in topographically modified barotropic semidiurnal Kelvin waves. J. Geophys. Res. Oceans 121, 3058–3074. https://doi.org/10.1002/2015JC011617.
Zhao, Z., Alford, M.H., Girton, J.B., Rainville, L., Simmons, H.L., 2016. Global observations of open-ocean mode-1 M2 internal tides. J. Phys. Oceanogr. 46, 1657–1684. https://doi.org/10.1175/JPO-D-15-0105.1.